Study of the density of electrons in momentum space in the Al - Li - Cu icosahedral phase by means of positron annihilation

1997 J. Phys.: Condens. Matter 9 11247

(http://iopscience.iop.org/0953-8984/9/50/025)

J. Phys.: Condens. Matter **9** (1997) 11247–11261. Printed in the UK PII: S0953-8984(97)87074-9

Study of the density of electrons in momentum space in the Al–Li–Cu icosahedral phase by means of positron annihilation

Yoshikazu Tanaka†§, Susumu Nanao† and Shoichiro Tanigawa‡

† Institute of Industrial Science, The University of Tokyo, Roppongi, Minato, Tokyo 106, Japan
‡ Institute of Materials Science, University of Tsukuba, Tsukuba, Ibaraki 305, Japan

Received 22 August 1997

Abstract. The three-dimensional momentum density of annihilating electron–positron pairs has been studied for a single Al–Li–Cu icosahedral quasicrystal. A direct Fourier transform method is employed to reconstruct the three-dimensional momentum density from measurements of the two-dimensional angular correlation of positron annihilation radiation (2D-ACAR). The crystallographic anisotropy in the momentum density is observed to be very small. The asphericity of the Fermi surface is not found explicitly within the experimental resolution in the momentum space. The features of the three-dimensional electron–positron momentum density agree with those obtained by means of Compton profile measurement. It is suggested that a strong lattice–electron interaction at the Fermi level occurs in this icosahedral phase.

1. Introduction

Since the discovery of quasicrystals, many investigations have been made of their crystallographic structures and electronic properties, experimentally and theoretically. One of the most interesting features of quasicrystals is the lack of translational periodicity in the atomic structures, which leads to the breakdown of the Bloch theorem and to the absence of Brillouin zones. Therefore, no plane-wave functions propagate in quasicrystals. Yet a lot of strong diffraction peaks are observed in the diffraction patterns of x-rays and electrons for quasicrystals because of the existence of the quasi-periodicity, i.e. long-range bond-orientational order with a non-crystallographic symmetry, such as the icosahedral point group symmetry.

The quasicrystal $Al_6Li_4Cu_1$, which is onre of the $(Al, Zn)_{49}Mg_{33}$-type (Frank–Kasper-type) icosahedral phases (i-phases), was discovered by Sainfort *et al* [1] and Ball and Lloyd [2]. It has been found that this i-phase forms in thermal equilibrium [3–5]. This i-phase is classified as a so-called s, p-electron quasicrystal because the valence band is dominated by the s, p electrons at the Fermi level. The stability of the i-phases has been discussed in terms of the number of valence electrons per atom (e/a) and other parameters by some researchers [6, 7]. It was pointed out that these s, p-electron quasicrystals can form when the value of e/a is close to 2.0, and that these stable i-phases obey the relation $Q \simeq 2k_F$, where Q is the diameter of the quasi-Brillouin zone and $2k_F$ is that of the Fermi surface

§ Present address: The Institute of Physical and Chemical Research (RIKEN), Hirosawa 2-1, Wako, Saitama 351-01, Japan; e-mail: ytanaka@postman.riken.go.jp.

0953-8984/97/5011247+15$19.50

[7]. The values of Q are evaluated from the most intense diffraction peak in the x-ray diffraction patterns, and the values of $2k_F$ are calculated from the free-electron model.

The electronic properties of the quasicrystals have been reported in the literature [8–10]. It has been found that the resistivities of the quasicrystals are quite high compared to those of conventional crystalline alloys. The temperature dependence of the specific heat in the Al–Li–Cu i-phase has indicated that the value of the density of states (DOS) at the Fermi energy is much smaller than that of the free-electron-gas model [11–13]. This result is consistent with the decrease of the peak height at the Fermi threshold in the soft-x-ray spectra [11]. From the electronic specific heat measurements for many s, p-electron quasicrystals and Frank–Kasper crystals, it is known that the ratio of the electronic specific heat coefficient to the value from the corresponding free-electron model becomes very small when the number of valence electrons per atom (e/a) approaches about 2.0 [14]. This result suggests that a pseudo-gap appears at the Fermi level in the DOS when the integrated DOS per atom approaches 2.0. It was argued that the stabilization of the Al–Li–Cu i-phase is due to the gain of the band-structural energy when a pseudo-gap exists at the Fermi level [14, 15]. On the basis of model calculations of the electronic structure of several crystalline approximants of quasicrystals, Fujiwara and Yokokawa have suggested that the DOS in the Al–Li–Cu quasicrystal probably has a pseudo-gap, and that the Fermi energy is located at the minimum of the DOS. For the electron–electron interaction, the weak localization is reported to be the cause of the temperature dependence of the resistivity and the magnetic field dependence of the magnetoresistance in the Al–Li–Cu i-phase [13].

In a Compton scattering study of the Al–Li–Cu i-phase [17], it was found that the number of valence electrons is much smaller than that for the electron gas model, and that the momentum density of the valence electrons has a long tail. It was concluded that the electronic structure of the i-phase is very different from that of the simple metal, and that a large proportion of the contribution from higher-momentum components is caused by the very strong electron–lattice interaction in the i-phase. In this paper, a study of the momentum density of electrons in an Al–Li–Cu i-phase by means of positron annihilation will be presented. Measurements of the two-dimensional angular correlation of positron annihilation radiation (2D-ACAR) were made, and the three-dimensional (3D) electron–positron momentum density was reconstructed by a direct Fourier transform method. The purpose of this study is to establish a description of the electronic system of the i-phase in terms of strong lattice–electron interaction and asphericity of the Fermi surface.

2. Experimental procedure

A single crystal of the Al–Li–Cu i-phase was grown at a rate of 0.5 mm per hour by the Bridgman method. The detail is described elsewhere [17]. A specimen for the 2D-ACAR experiment was cut out from the single i-phase block. The specimen was chemically etched with dilute nitric acid. The specimen was 15 mm in diameter and 0.4 mm in thickness. The composition of the phase was found by analysis to be $Al_{59.3}Li_{9.3}Cu_{11.4}$ (atomic percentages), by means of inductively coupled plasma spectrometry.

The 3D momentum space of the i-phase, which has icosahedral symmetry, can be divided into 60 independent spherical sections, each of which has five-, three-, and twofold axes at its three corners. One of the fivefold axes was taken as the direction of the incident positron beam. Then couples of γ-rays of positron annihilation were emitted perpendicular to this fivefold axis. The 2D-ACAR spectra were measured for seven projections by rotating the sample around the fivefold axis in six-degree steps in order to reconstruct the 3D electron–positron momentum density. This total rotation of 36° covers one of the independent solid

angles of the momentum space. The experimental system is described in detail elsewhere [18]. A total of about 6×10^7 counts were accumulated for one ACAR spectrum.

3. Reconstruction

The 2D-ACAR spectrum

$$N(p_y, p_z) = \int \rho(\boldsymbol{p})\ \mathrm{d}p_x \tag{3.1}$$

is a one-dimensional projection of the momentum density $\rho(\boldsymbol{p})$ onto planes perpendicular to the direction of the emitted γ-rays, where $\boldsymbol{p}$ is the annihilating electron–positron momentum. For convenience, the coordinates on the x-, y-, and z-axes are given with respect to the sample, and the normal vectors of the planes of the seven 2D-ACAR spectra are written as $(x_i, y_i, z_i), i = 1, 2, \ldots, 7$. In the measurements, the z-axis was for all of the 2D-ACAR spectra fixed along one of the fivefold axes of the Al–Li–Cu i-phase, and the sample was rotated in the xy-plane in six-degree steps in every measurement. The coordinates are determined as follows. Firstly, the z-axis is set to the direction of the incident positron beam, which is along one of the fivefold axes. Secondly, the x-axis is set so that another fivefold axis lies in the xz-plane. Then the directions of the six independent fivefold vectors are $(0, 0, 1)$, $(2t, 0, t)$, $(2t\cos 2\pi/5, 2t\sin 2\pi/5, t)$, $(2t\cos 4\pi/5, 2t\sin 4\pi/5, t)$, $(2t\cos 6\pi/5, 2t\sin 6\pi/5, t)$, and $(2t\cos 8\pi/5, 2t\sin 8\pi/5, t)$. Here, t is $1/\sqrt{5}$. The normal vectors, $(x_i, y_i, z_i), i = 1, 2, \ldots, 7$, of the planes of the seven 2D-ACAR spectra are $(0, 1, 0)$, $(-\sin\pi/30, \cos\pi/30, 0)$, $(-\sin 2\pi/30, \cos 2\pi/30, 0)$, $(-\sin 3\pi/30, \cos 3\pi/30, 0)$, $(-\sin 4\pi/30, \cos 4\pi/30, 0)$, $(-\sin 5\pi/30, \cos 5\pi/30, 0)$, and $(-\sin 6\pi/30, \cos 6\pi/30, 0)$.

A direct Fourier transform method was used to reconstruct the 3D electron–positron momentum density $\rho(\boldsymbol{p})$ in the following way. The 3D Fourier transform of $\rho(\boldsymbol{p})$, $B(\boldsymbol{r})$, is written as

$$B(\boldsymbol{r}) = (2\pi)^{-3/2} \int\int\int \rho(\boldsymbol{p}) \exp(-\mathrm{i}\boldsymbol{p}\cdot\boldsymbol{r})\ \mathrm{d}\boldsymbol{p}. \tag{3.2}$$

Conversely, $\rho(\boldsymbol{p})$ is obtained from $B(\boldsymbol{r})$ with the aid of the inverse transform. Assuming that the normal vector of a 2D-ACAR spectrum is chosen along the x-axis and setting $x = 0$, it follows from equation (3.1) that

$$B(0, y, z) = (2\pi)^{-3/2} \int\int N(p_y, p_z) \exp\left[-\mathrm{i}(yp_y + zp_z)\right] \mathrm{d}p_y\ \mathrm{d}p_z. \tag{3.3}$$

Thus, the 2D Fourier transform of a 2D-ACAR spectrum gives the values of $B(\boldsymbol{r})$ on the yz-plane directly. By varying the direction of the normal vector of a 2D-ACAR spectrum, the transformed function $B(\boldsymbol{r})$ is determined on many planes through its origin. A brief outline of the direct Fourier transform method is as follows. The 2D-ACAR data measured for seven directions are firstly Fourier transformed. This procedure gives seven sets of the values of $B(\boldsymbol{r})$, on the seven corresponding planes. Secondly the sets of data give the 3D $B(\boldsymbol{r})$ by interpolation onto a cubic grid of the $B(\boldsymbol{r})$, and, finally, 3D inverse Fourier transformation of $B(\boldsymbol{r})$ gives the full 3D momentum density $\rho(\boldsymbol{p})$.

In the case of the i-phase, there is some difficulty in the calculation of the Fourier transform. When the sample has a simple cubic lattice, such as a face-centred cubic one, the Fourier transformation can easily be performed in real space. In the icosahedral system, however, it is presumed that $\rho(\boldsymbol{p})$ is a simple point-symmetric function in the calculation. Although the Fourier transform of a point-symmetric 2D function becomes

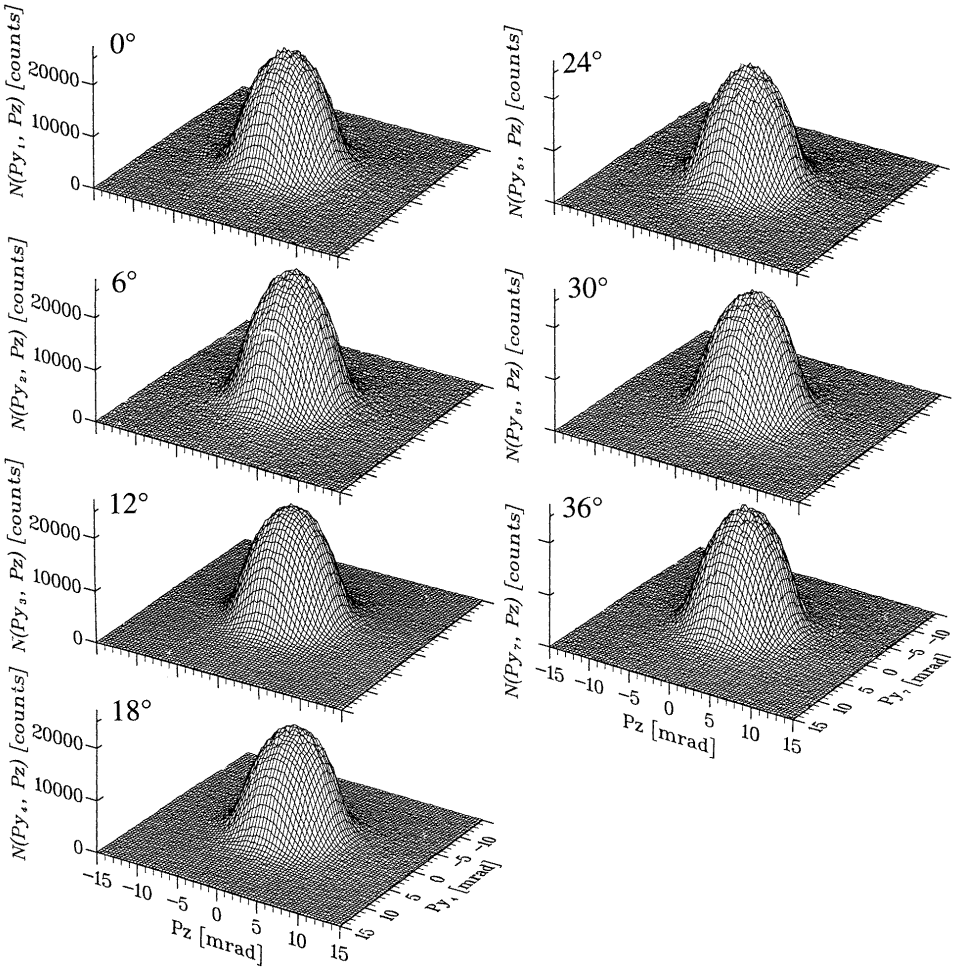

Figure 1. The 2D-ACAR spectra of the Al–Li–Cu icosahedral phase for seven projections. The vector represents the normal vector for each of the planes. The angle denotes the deviation of the normal vectors from the y-axis.

a real function (see appendix A), a direct calculation of the Fourier transform should be carried out in complex space. The computation of the Fourier transform in complex space requires a great deal of time and memory. A method for calculating the Fourier transform of a point-symmetric 2D function has been developed to facilitate carrying out the Fourier transformation in real space. The details are described in appendix A. Before the 2D Fourier transformation, each of the 2D-ACAR spectra was folded, with the origin $p_y = p_z = 0$, in order to obtain the point-symmetric $N(p_y, p_z)$. Secondly, each spectrum was Fourier transformed using the method described in appendix A. Then the seven sets of data on the planes in $B(\boldsymbol{r})$ were obtained. Thirdly, a 3D mesh of $B(\boldsymbol{r})$ was determined so that the interval of the neighbouring mesh points was $\pi/25.4$ mrad^{-1}; this value was thus set to be a little smaller than half of the period of the maximum momentum value (20 mrad) in the measurement, for precise interpolation. The seven sets of data were arranged on the 3D mesh according to the icosahedral symmetry. In total, 60 sets of data for the planes

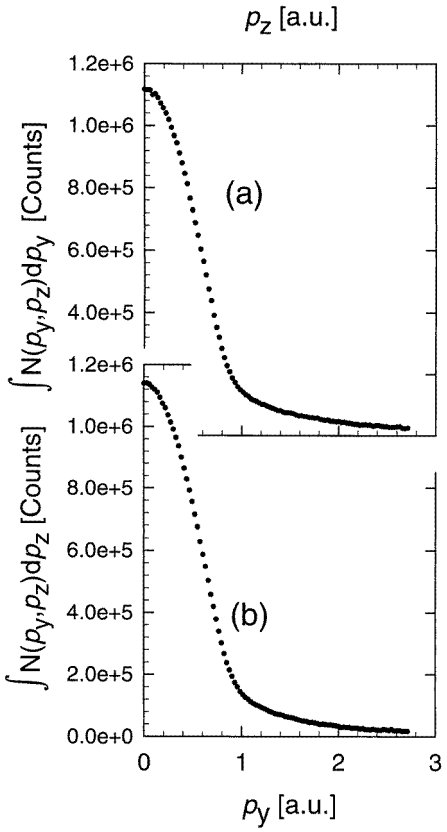

Figure 2. The integrated momentum density along (a) the fivefold axis and (b) the other axis perpendicular to the fivefold axis of the 2D-ACAR spectrum indexed by $i = 7$.

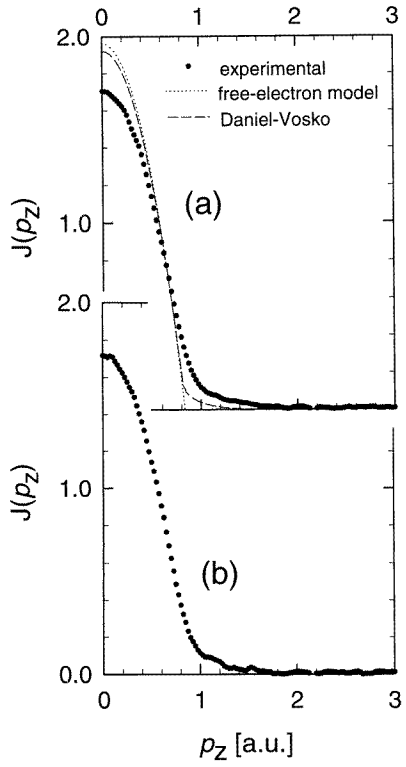

Figure 3. The Compton profiles along the (a) fivefold and (b) twofold axes of the Al–Li–Cu icosahedral phase. The dotted line represents the parabola of the electron gas model. The broken line is the Compton profile of the valence electron simulated on the basis of Daniel and Vosko's theory.

covered the 3D mesh of $B(\boldsymbol{r})$. The value at each mesh point was calculated by means of a 3D spline interpolation using the values on the 60 2D $B(\boldsymbol{r})$ planes. Finally, the 3D $\rho(\boldsymbol{p})$ was obtained using the inverse 3D Fourier transformation described in appendix B.

4. Results and discussion

In the independent-particle model, the electron–positron momentum density $\rho(\boldsymbol{p})$ can be written as

$$\rho(\boldsymbol{p}) = \sum_{n,\boldsymbol{k}}^{\text{occ.}} \left| \int_V \mathrm{d}\boldsymbol{r}\ \psi_+(\boldsymbol{r})\psi_{n,\boldsymbol{k}}(\boldsymbol{r}) \exp(-\mathrm{i}\boldsymbol{r}\cdot\boldsymbol{p}) \right|^2 \tag{4.1}$$

where $\psi_{n,\boldsymbol{k}}$ is the wave function of an electron, n the band index, $\boldsymbol{k}$ the wave vector, $\psi_+(\boldsymbol{r})$ the wave function of a thermalized positron ($\boldsymbol{k} = 0$), V the crystal volume, and the summation is taken over all of the occupied electron states. The 2D-ACAR spectrum measured in the experiment is a onefold integral of $\rho(\boldsymbol{p})$ as represented by equation (3.1),

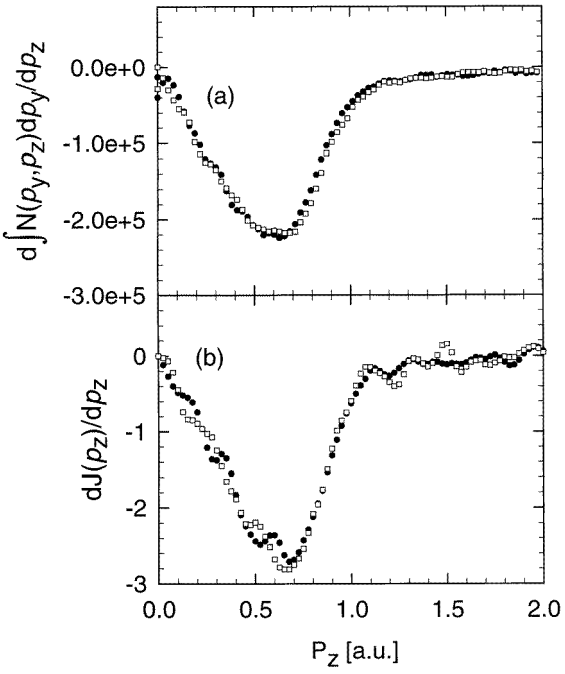

Figure 4. (a) The first derivatives of the integrated momentum densities along the fivefold axis (dots) and the axis perpendicular to the fivefold axis (squares) for the 2D-ACAR spectrum indexed by $i = 7$. (b) The first derivatives of the Compton profiles along the fivefold (dots) and twofold axes (squares).

and the spectra measured for the Al–Li–Cu icosahedral single crystal are shown in figure 1. Each spectrum has a peak at $\boldsymbol{p} = 0$ contributed by the valence electrons. These spectra do not show any apparent anisotropic feature in the momentum space. The *z*-axes of the various panels of the figure each correspond to one of the fivefold axes. The 2D-ACAR spectra were integrated along the *z*-axes and the *y*-axes respectively in order to compare the Compton profiles measured previously for the same sample. Figure 2 shows the integrated momentum densities along the *z*-axis and the *y*-axis of the 2D-ACAR spectrum indexed by $i = 7$. The momentum scale, milliradians (mrad), for the 2D-ACAR spectrum was converted to atomic units (au) by multiplying by the factor $\overline{h}c/1000e^2 = 0.137$. The momentum density of the valence electrons is observed to be a parabolic curve from 0 au to about 0.8 au. The momentum density of the core electrons is observed as long tails above about 2 au. In a simple free-electron model, its twofold-integrated momentum density would lie on a parabolic curve. To evaluate the contribution of the core electrons, the integrated 2D-ACAR spectra of all of the directions were averaged and fitted to a theoretical momentum distribution (Compton profile) of the core electrons based on the free-atom Hartree–Fock calculation [20]. The amount of the contribution was estimated to be about 17% from -2.7 au to 2.7 au.

The Compton profile, $J(p_z)$, is written as

$$J(p_z) = \int\int \sum_{\boldsymbol{n},\boldsymbol{k}}^{\text{occ.}} \left| \int_V \mathrm{d}\boldsymbol{r}\ \psi_{\boldsymbol{n},\boldsymbol{k}}(\boldsymbol{r}) \exp(-\mathrm{i}\boldsymbol{r}\cdot\boldsymbol{p}) \right|^2 \mathrm{d}p_x\ \mathrm{d}p_y. \tag{4.2}$$

The Compton profile is a twofold integral of the electron momentum density, which essentially gives the same information as a 2D-ACAR spectrum, except that the Compton profile does not include positron wave functions. Hence, the Compton profile is free from the unknown positron wave functions. The Compton profiles [17] of the valence electrons of the same sample are shown in figure 3.

Table 1. The momentum values (au) of the peak positions in the second derivatives of the integrated electron–positron momentum densities of the 2D-ACAR spectrum indexed by $i = 7$ and those of the Compton profiles.

		The value of the momentum
The electron–positron momentum density	$\parallel$ fivefold axis	0.83 ± 0.04
	$\perp$ fivefold axis	0.82 ± 0.04
The Compton profiles	Fivefold axis	0.87 ± 0.10
	Twofold axis	0.87 ± 0.10

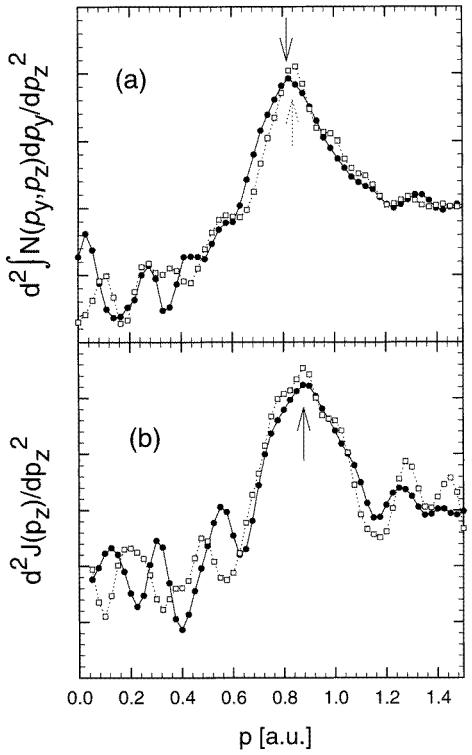

Figure 5. (a) The second derivatives of the integrated momentum densities along the fivefold axis (dots) and the axis perpendicular to the fivefold axis (squares) for the 2D-ACAR spectrum indexed by $i = 7$. (b) The second derivatives of the Compton profiles along the fivefold (dots) and twofold axes (squares). Arrows denote the positions at which the maxima of the peaks appear.

To examine the momentum density around the Fermi surface and to compare the electron–positron momentum density with the electron momentum density obtained from the Compton profiles, the first and second derivatives of the integrated electron–positron momentum densities and the Compton profiles were derived. The first derivatives are shown in figure 4. Although the first derivatives of the integrated momentum densities are very similar to those of the Compton profiles, the shapes of the bottoms of these are slightly different from those of the Compton profiles. The second derivatives of those profiles are shown in figure 5. The positions at which the maxima of the peaks appear in the second derivatives of the Compton profiles have almost the same values of the Fermi radii as those evaluated by fitting the Compton profiles to parabolas [17]. These momentum values are summarized in table 1. The positions at which the maxima of the peaks appear in the second derivatives of the integrated electron–positron momentum densities have slightly smaller momentum values than those of the Compton profiles.

Table 2. The values of the momenta (au) of the peaks of the first derivatives of the electron–positron momentum density and the Fermi radii of the Compton profiles. Here, t is $1/\sqrt{5}$ and u is $(\sqrt{5}+1)/2$. The values of p_{5-avr} and p_{2-avr} are the average values of momenta along the fivefold axes and twofold axes, respectively.

The electron–positron momentum density	Fivefold axes	[0, 0, 1]	0.780 ± 0.04
		$[2t, 0, t]$	0.810 ± 0.04
		$[2t\cos 2\pi/5, 2t\sin 2\pi/5, t]$	0.790 ± 0.04
		$[2t\cos 4\pi/5, 2t\sin 4\pi/5, t]$	0.795 ± 0.04
		$[2t\cos 6\pi/5, 2t\sin 6\pi/5, t]$	0.780 ± 0.04
		$[2t\cos 8\pi/5, 2t\sin 8\pi/5, t]$	0.785 ± 0.04
	p_{5-avr}		0.790 ± 0.04
	Twofold axes	[0, 1, 0]	0.788 ± 0.04
		$[\cos 9\pi/10, \sin 9\pi/10, 0]$	0.788 ± 0.04
		$[\cos 13\pi/10, \sin 13\pi/10, 0]$	0.791 ± 0.04
		$[\cos 17\pi/10, \sin 17\pi/10, 0]$	0.790 ± 0.04
		$[\cos \pi/10, \sin \pi/10, 0]$	0.798 ± 0.04
		$[-u, 0, 1]$	0.812 ± 0.04
		$[u\cos 14\pi/10, u\sin 14\pi/10, 1]$	0.784 ± 0.04
		$[u\cos 18\pi/10, u\sin 18\pi/10, 1]$	0.790 ± 0.04
		$[u\cos 2\pi/10, u\sin 2\pi/10, 1]$	0.805 ± 0.04
		$[u\cos 6\pi/10, u\sin 6\pi/10, 1]$	0.810 ± 0.04
		$[1, 0, u]$	0.810 ± 0.04
		$[\cos 4\pi/10, \sin 4\pi/10, u]$	0.812 ± 0.04
		$[\cos 8\pi/10, \sin 8\pi/10, u]$	0.810 ± 0.04
		$[\cos 12\pi/10, \sin 12\pi/10, u]$	0.795 ± 0.04
		$[\cos 16\pi/10, \sin 16\pi/10, u]$	0.815 ± 0.04
	p_{2-avr}		0.800 ± 0.04
The Compton profiles[a]	Fivefold axis		0.862 ± 0.1
	Twofold axis		0.861 ± 0.1
The electron gas model			0.835

[a] Adapted from reference [17].

The 3D electron–positron momentum density was reconstructed from the 2D-ACAR spectra using the method described in section 3. On the assumption that the momentum density of the core electrons is isotropic, the 3D momentum density of the core electrons was also reconstructed independently, and was subtracted from the total 3D electron–positron momentum density. The contribution of the core electrons at $\boldsymbol{p} = 0$ au to the total

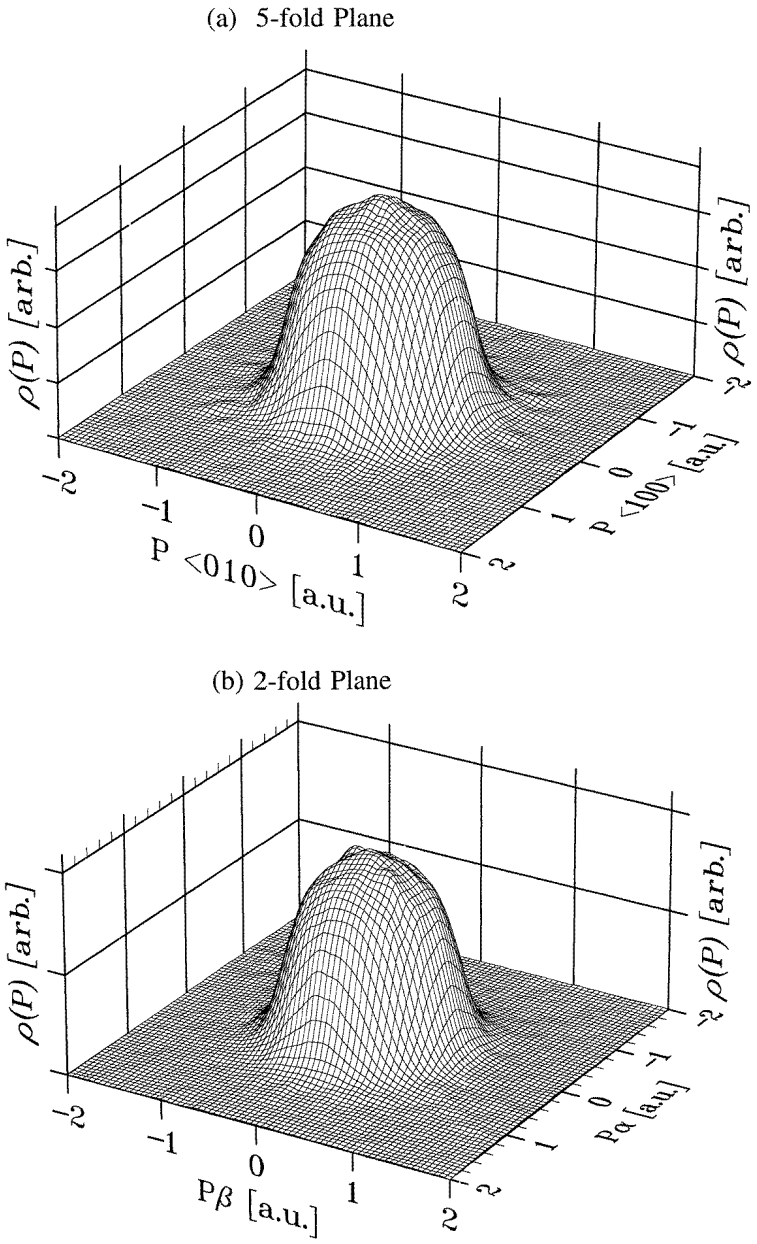

Figure 6. (a) A cross-section of a plane perpendicular to one of the fivefold axes represented by the z-axis [001]. (b) A cross-section of a plane perpendicular to one of the twofold axes represented by the y-axis [010]. Here, the α- and β-axes represent twofold axes, $[-(\sqrt{5}+1)/2, 0, 1]$ and $[1, 0, (\sqrt{5}+1)/2]$, respectively.

momentum density was evaluated to be 0.7%. The two cross-sections of the reconstructed momentum density $\rho(\boldsymbol{p})$ shown in figure 6 suggest that the momentum density is almost spherical. To evaluate the asphericity of the Fermi surface and the Fermi radii in the principal directions, the momentum densities and their first derivatives on all of the fivefold

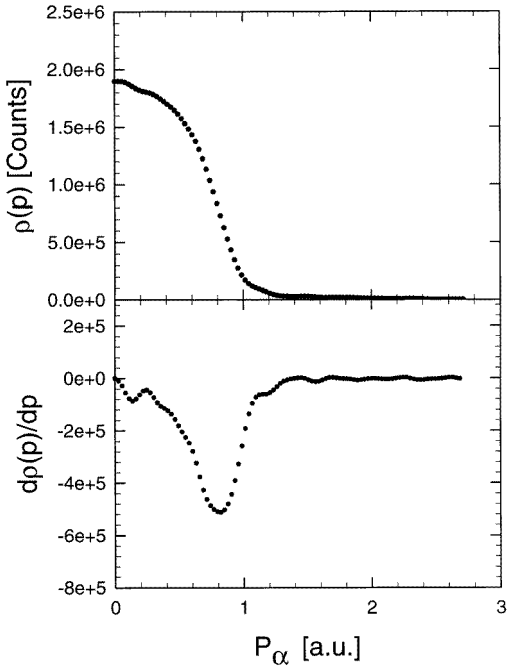

(a)

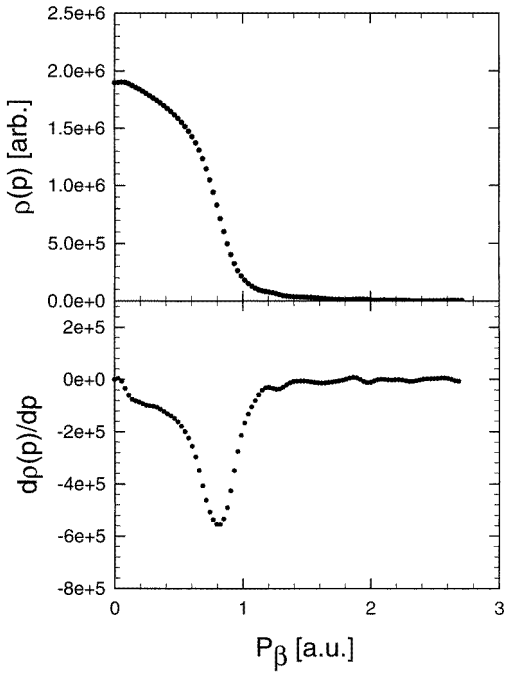

(b)

Figure 7. (a) The momentum density on the twofold axis represented by the vector $[-(\sqrt{5}+1)/2, 0, 1]$ and its first derivative. (b) The momentum density on the twofold axis represented by the vector $[1, 0, (\sqrt{5}+1)/2]$ and its first derivative.

axes and all of the twofold axes were derived. The results are shown in figure 7. In a simple free-electron model, its momentum density would show a step function according to the Fermi–Dirac statistics. A smearing of the momentum density at the Fermi surface and long tails are observed in all of the directions. Each of the first derivatives has a broad peak around the Fermi surface. The values of momenta at which the peaks of the first derivatives appear are listed in table 2. The average value almost coincides with those evaluated in figure 5.

In the electron gas scheme, these values can be defined as Fermi radii. It was found that there is a very small anisotropic feature in the Fermi surface of the electron–positron momentum density. The value for an electron gas model is calculated on the assumption of three electrons for Al, one electron for Li, and one electron for Cu. As seen in table 2, the value of the Fermi radius of the model is slightly larger than those of the electron–positron momentum densities and slightly smaller than those of the Compton profiles.

We have introduced the following parameter, δ:

$$\delta = (p_{2-avr} - p_{5-avr})/p_{avr} \tag{4.3}$$

in order to describe the deviation of the Fermi surface from sphericity. Here, p_{2-avr} and p_{5-avr} are the average values of momenta at which the peaks of the first derivatives appear along the twofold axes and fivefold axes, respectively, and p_{avr} is the total average value. δ was evaluated to be 1.3%. The resolution of the momentum in the measurement is 0.2 mrad, which corresponds to 3.4% of p_{avr}. Although the values of the Fermi radii along the twofold axes are slightly larger than those of the Fermi radii along the fivefold axes, the asphericity of the Fermi surface is not explicit within the experimental resolution. The above results are summarized as follows: (1) the value of the Fermi radius of the electron gas model is slightly larger than those obtained from the electron–positron momentum densities and slightly smaller than those obtained from the Compton profiles; (2) the asphericity of the Fermi surface is not obvious within the experimental resolution.

Table 3. The values of the momenta (au) of the cross-sections at which the quasi-Brillouin-zone boundaries cut the five-, three-, and twofold axes [17].

	Fivefold axis	Twofold axis	Threefold axis
(221001)	0.867	0.737	0.789
(222100)	0.997	0.848	0.853

These results can be explained as follows. In the Compton profile experiment, it was found that the simple electron gas model cannot explain the experimental profiles, and it was suggested that the wave functions of the valence electrons at the Fermi level are far from being simple plane waves. One of the reasons for this is that the strong electron–lattice interaction occurs at the Fermi level in the i-phase. Taking the Umklapp process into account, the momentum density $\rho(\boldsymbol{p})$ in a normal crystal is written as

$$\rho(\boldsymbol{p}) = \sum_{n,k}^{\text{occ.}} \sum_{G} \left| A_{n,k}(\boldsymbol{G}) \right|^2 \delta_{\boldsymbol{p}-\boldsymbol{k},\boldsymbol{G}} \tag{4.4}$$

where the $A_{n,k}(\boldsymbol{G})$ are the Fourier coefficients of the Bloch part of the wave functions. It was pointed out that the values of the momenta of the quasi-Brillouin-zone boundaries estimated from the strong x-ray diffraction peaks (221001) and (222100) [19] are very close to that of the Fermi surface. The symmetries of the quasi-Brillouin-zone boundaries corresponding to the (221001) and (222001) peaks are those of a triacontahedron and

a hexacontahedron, respectively [17]. The values of the momenta of the cross-sections at which the quasi-Brillouin-zone boundaries cut the five-, three-, and twofold axes are summarized in table 3. These two boundaries form an approximately spherical boundary. This spherical boundary can enhance the electron–lattice interaction because it is very close to the Fermi surface. From the band calculations for the crystal that is an approximant for the Al–Li–Cu i-phase, it is predicted that the strong electron–lattice interaction causes a pseudo-gap at the Fermi energy [16]. Thus, the long tails that appeared in the 3D electron–positron momentum density as well as those in the Compton profiles are attributable to a large contribution from the higher-momentum components, $\boldsymbol{G} \neq 0$, in equation (4.4), in the Umklapp process, owing to the strong electron–lattice interaction. The above discussion supports the existence of the pseudo-gap indirectly; this can explain various results from the experiments regarding the electronic properties of the i-phase, such as the electrical resistivity [12–14], specific heat [12–14], and magnetoresistance [13].

If the wave functions of the valence electrons were localized in real space, they would appear to be extended in momentum space, and the momentum density would not be explained in the electron gas scheme, whereas, in fact, this experimental result as well as those of the Compton scattering experiment have at least the Fermi cut-off feature in the momentum density, and do not indicate any signature of localization of the valence electrons. These experimental results support the existence of a pseudo-gap at the Fermi level. However, it is difficult to discuss the mobility of the valence electrons purely on the basis of these experiments on the momentum density, The low electronic conductivity of the i-phase may be explicable in two ways: as being caused by the large effective mass of the valence electrons or as being caused by the small value of the density of states at the Fermi level. Our experimental results support the latter explanation.

The difference between the results from the 2D-ACAR spectra and the Compton profiles are explained as follows: the incident x-rays have equivalent cross-sections for all of the electrons in a sample within the impulse approximation in the Compton scattering, whereas the probability of the electron–positron annihilation depends on the kind of electron—such as core electrons and valence electrons—because the positron wave functions do not have a uniform amplitude in the sample. The positron wave functions have larger amplitude, i.e. the electron–positron annihilation occurs at a higher rate, in regions where the ion density is smaller or the electron density is smaller. This effect makes the values of the Fermi radii smaller for the sample with vacancy-like defects. In the case of a sample free from crystalline defects, the above effect is not observed. The positron lifetime spectra reported for the Al–Li–Cu i-phase [21], however, reveal the existence of three lifetime components. The intensity of the principal lifetime, $\tau_2 = 205 \pm 4$ ps, which can be attributed to a dense concentration of vacancy-like defects, is about 80%. It was reported on the basis of x-ray and neutron diffraction experiments on the Al–Li–Cu crystalline approximant (the R phase) [22] that the central site of the icosahedral clusters in the R phase is vacant. A band-structural calculation [16] also reported that if the central site of the icosahedral clusters is not vacant, the R phase does not stabilize energetically. In the positron lifetime study, it is suggested that the Al–Li–Cu i-phase has the same icosahedral clusters as the crystalline phase, and that the central sites of the icosahedral clusters possibly offer vacancy-like defects.

5. Conclusion

The 3D electron–positron momentum density of the Al–Li–Cu i-phase was found to be almost isotropic. The parameter δ for the anisotropy is evaluated to be about $1.3 \pm 3.4\%$, which means that the asphericity of the Fermi surface is not obvious within the experimental

resolution. The long tails that appeared in the 3D electron–positron momentum density for valence electrons are attributed to the large contribution from the high-momentum components generated by the Umklapp process due to the strong electron–lattice interaction. The Fermi cut-off feature is clearly observed, which indicates that the valence electrons have Bloch-electron-like characteristics for the most part. No signatures of localized states or critical states of the valence electrons were observed. The values of the Fermi radii obtained by means of positron annihilation are slightly smaller than those obtained by means of Compton scattering. The large number of intrinsic defects in the Al–Li–Cu i-phase have probably led to the difference between the results obtained from the positron annihilation and the Compton scattering.

Acknowledgment

The authors wish to express their thanks to Dr Y Sakurai of the Institute of Physical and Chemical Research (RIKEN) for his help in carrying out the experiments.

Appendix A. The 2D Fourier transform of a point-symmetric function

A 2D point-symmetric function $f(x, y)$ can be expressed as

$$f(x, y) = f(-x, -y). \tag{A.1}$$

This function $f(x, y)$ can be divided into two parts, $c(x, y)$ and $s(x, y)$. These functions are related as follows:

$$f(x, y) = c(x, y) + s(x, y) \tag{A.2a}$$

$$c(x, y) = \frac{1}{2}[f(x, y) + f(-x, y)] \tag{A.2b}$$

$$s(x, y) = \frac{1}{2}[f(x, y) - f(-x, y)]. \tag{A.2c}$$

The properties of the functions $c(x, y)$ and $s(x, y)$ are expressed as

$$c(x, y) = c(\pm x, \pm y) \tag{A.3a}$$

$$s(x, y) = -s(-x, y) = -s(x, -y) = s(-x, -y) \tag{A.3b}$$

which are deduced from equation (A.1). The function $c(x, y)$ is even with respect to the planes $x = 0$ and $y = 0$, and the function $s(x, y)$ is odd with respect to the planes $x = 0$ and $y = 0$.

The Fourier transform of $f(x, y)$ is written as

$$F(p_x, p_y) = \int_{-\infty}^{\infty}\int_{-\infty}^{\infty} f(x, y) \exp[-\mathrm{i}(xp_x + yp_y)]\ \mathrm{d}x\ \mathrm{d}y. \tag{A.4}$$

This function can also be divided into two parts, $C(p_x, p_y)$ and $S(p_x, p_y)$. The function $F(p_x, p_y)$ is expressed as

$$F(p_x, p_y) = C(p_x, p_y) - S(p_x, p_y). \tag{A.5}$$

The functions $C(p_x, p_y)$ and $S(p_x, p_y)$ are the Fourier transforms of $c(x, y)$ and $s(x, y)$, respectively. These Fourier transforms are written as

$$C(p_x, p_y) = 4\int_0^{\infty}\int_0^{\infty} c(x, y)\cos(xp_x)\cos(yp_y)\ \mathrm{d}x\ \mathrm{d}y \tag{A.6a}$$

$$S(p_x, p_y) = 4\int_0^{\infty}\int_0^{\infty} s(x, y)\sin(xp_x)\sin(yp_y)\ \mathrm{d}x\ \mathrm{d}y. \tag{A.6b}$$

All of these functions are real. The imaginary part of $F(\boldsymbol{p})$ cancels out in the integral because the integrand is odd; for example,

$$f(x, y)\cos(xp_x)\sin(yp_y) = -f(-x, -y)\cos(-xp_x)\sin(-yp_y). \tag{A.7}$$

This scheme can be extended to higher-dimensional Fourier transforms.

Appendix B. The 3D Fourier transform of a point-symmetric function

A 3D point-symmetric function $f(x, y, z)$ can be expressed as

$$f(x, y, z) = f(-x, -y, -z). \tag{B.1}$$

This function $f(x, y, z)$ can be divided into four parts, $c(x, y, z)$, $s_x(x, y, z)$, $s_y(x, y, z)$, and $s_z(x, y, z)$. These functions are related as follows:

$$f(\boldsymbol{r}) = c(\boldsymbol{r}) + s_x(\boldsymbol{r}) + s_y(\boldsymbol{r}) + s_z(\boldsymbol{r}) \qquad \boldsymbol{r} = (x, y, z) \tag{B.2a}$$

$$c(x, y, z) = \frac{1}{4}[f(x, y, z) + f(-x, y, z) + f(x, -y, z) + f(x, y, -z)] \tag{B.2b}$$

$$s_x(x, y, z) = \frac{1}{4}[f(x, y, z) + f(-x, y, z) - f(x, -y, z) - f(x, y, -z)] \tag{B.2c}$$

$$s_y(x, y, z) = \frac{1}{4}[f(x, y, z) - f(-x, y, z) + f(x, -y, z) - f(x, y, -z)] \tag{B.2d}$$

$$s_z(x, y, z) = \frac{1}{4}[f(x, y, z) - f(-x, y, z) - f(x, -y, z) + f(x, y, -z)]. \tag{B.2e}$$

The properties of the functions $c(\boldsymbol{r})$, $s_x(\boldsymbol{r})$, $s_y(\boldsymbol{r})$, and $s_z(\boldsymbol{r})$ are expressed as follows:

$$c(x, y, z) = c(\pm x, \pm y, \pm z) \tag{B.3a}$$

$$s_x(x, y, z) = s_x(-x, y, z) = -s_x(x, -y, z) = -s_x(x, y, -z) \tag{B.3b}$$

$$s_y(x, y, z) = -s_y(-x, y, z) = s_y(x, -y, z) = -s_y(x, y, -z) \tag{B.3c}$$

$$s_z(x, y, z) = -s_z(-x, y, z) = -s_z(x, -y, z) = s_z(x, y, -z). \tag{B.3d}$$

These expressions are deduced from equation (B.1). The functions $s_x(\boldsymbol{r})$, $s_y(\boldsymbol{r})$, and $s_z(\boldsymbol{r})$ are even with respect to the planes $x = 0$, $y = 0$, and $z = 0$, respectively, and odd with respect to the other two planes from among $x = 0$, $y = 0$, and $z = 0$.

The Fourier transform of $f(\boldsymbol{r})$ is written as

$$F(\boldsymbol{p}) = \int_{-\infty}^{\infty}\int_{-\infty}^{\infty}\int_{-\infty}^{\infty} f(\boldsymbol{r})\exp[-\mathrm{i}(\boldsymbol{r}\cdot\boldsymbol{p})]\,\mathrm{d}\boldsymbol{r}. \tag{B.4}$$

This function can be also divided into four parts, $C(\boldsymbol{p})$, $S_x(\boldsymbol{p})$, $S_y(\boldsymbol{p})$, and $S_z(\boldsymbol{p})$. The function $F(\boldsymbol{p})$ is expressed as

$$F(\boldsymbol{p}) = C(\boldsymbol{p}) - S_x(\boldsymbol{p}) - S_y(\boldsymbol{p}) - S_z(\boldsymbol{p}). \tag{B.5}$$

The functions $C(\boldsymbol{p})$, $S_x(\boldsymbol{p})$, $S_y(\boldsymbol{p})$, and $S_z(\boldsymbol{p})$ are the Fourier transforms of $c(\boldsymbol{r})$, $s_x(\boldsymbol{r})$, $s_y(\boldsymbol{r})$, and $s_z(\boldsymbol{r})$, respectively. These Fourier transforms are written as

$$C(\boldsymbol{p}) = 8\int_0^{\infty}\int_0^{\infty}\int_0^{\infty} c(\boldsymbol{r})\cos(xp_x)\cos(yp_y)\cos(zp_z)\,\mathrm{d}x\,\mathrm{d}y\,\mathrm{d}z \tag{B.6a}$$

$$S_x(\boldsymbol{p}) = 8\int_0^{\infty}\int_0^{\infty}\int_0^{\infty} s_x(\boldsymbol{r})\cos(xp_x)\sin(yp_y)\sin(zp_z)\,\mathrm{d}x\,\mathrm{d}y\,\mathrm{d}z \tag{B.6b}$$

$$S_y(\boldsymbol{p}) = 8\int_0^{\infty}\int_0^{\infty}\int_0^{\infty} s_y(\boldsymbol{r})\sin(xp_x)\cos(yp_y)\sin(zp_z)\,\mathrm{d}x\,\mathrm{d}y\,\mathrm{d}z \tag{B.6c}$$

$$S_z(\boldsymbol{p}) = 8\int_0^{\infty}\int_0^{\infty}\int_0^{\infty} s_z(\boldsymbol{r})\sin(xp_x)\sin(yp_y)\cos(zp_z)\,\mathrm{d}x\,\mathrm{d}y\,\mathrm{d}z. \tag{B.6d}$$

All of these functions are real. The imaginary part of $F(\boldsymbol{p})$ cancels out in the integration for the same reason as in the case of section 5.

References

[1] Sainfort P, Dubost B and Dubus A 1985 *C. R. Acad. Sci., Paris* **301** 689
[2] Ball M D and Lloyd D J 1985 *Scr. Metall.* **19** 1065
[3] Sainfort P and Dubost B 1986 *J. Physique* **47** C3 321
[4] Cassada W A, Shiflet G J and Poon S J 1986 *Phys. Rev. Lett.* **56** 2276
[5] Marcus M A and Elser V 1986 *Phil. Mag.* B **54** L101
[6] Villars P, Phillips J C and Chen H S 1986 *Phys. Rev. Lett.* **57** 3085
[7] Tsai A P, Inoue A and Masumoto T 1989 *Mater. Trans. Japan Inst. Met.* **30** 666
[8] Steinhart P J and Ostlund S (ed) 1987 *The Physics of Quasicrystals* (Singapore: World Scientific)
[9] Kimura K and Takeuchi S 1991 *Quasicrystals: The State of the Art* ed D P DiVincenzo and P Steinhardt (Singapore: World Scientific) p 313
[10] Poon S J 1992 *Adv. Phys.* **4** 303
[11] Bruhwiler P A, Wagner J L, Biggs B D, Shen Y, Wong K M, Schnatterly S E and Poon S J 1988 *Phys. Rev.* B **37** 6529
[12] Wagner J L, Biggs B D, Wong K M and Poon S J 1988 *Phys. Rev.* B **38** 7436
[13] Kimura K, Iwahashi H, Hashimoto T, Takeuchi S, Mizutani U, Ohashi S and Itoh G 1989 *J. Phys. Soc. Japan* **58** 2472
[14] Mizutani U, Kamiya A, Matsuda T, Kishi K and Takeuchi S 1991 *J. Phys.: Condens. Matter* **3** 3711
[15] Kishi K, Kimura K, Hashimoto T and Takeuchi S 1990 *J. Phys. Soc. Japan* **59** 1158
[16] Fujiwara T and Yokokawa T 1991 *Phys. Rev. Lett.* **66** 333
[17] Tanaka Y, Sakurai Y, Nanao S, Shiotani N, Ito M, Sakai N, Kawata H and Iwazumi T 1994 *J. Phys. Soc. Japan* **63** 3349
[18] Suzuki R, Osawa M, Tanigawa S, Matsumoto M and Shiotani N 1989 *J. Phys. Soc. Japan* **58** 3251
[19] Tanaka Y, Sakurai Y, Watanabe Y, Koshiba S and Nanao S 1989 *MRS Int. Mtg on Advanced Materials* vol 3 (Pittsburgh, PA: Materials Research Society Press) p 347
[20] Biggs F, Mendelsohn L B and Mann J B 1975 *At. Data Nucl. Data Tables* **16** 201
[21] Ohata T, Kanazawa I, Iwashita T, Kishi K and Takeuchi S 1990 *Phys. Rev.* B **42** 6730
[22] Guryan C A, Stephens P W, Goldman A I and Gayle F W 1988 *Phys. Rev.* B **37** 8495